Characterization and evolution of seismic sequences in the normal fault environment of the Southern Apennines

Francesco Scotto di Uccio [1], ***Maddalena Michele*** [2], ***Claudio Strumia*** [1], ***Mariano Supino*** [2], ***Gregory C. Beroza*** [3], ***Lauro Chiaraluce*** [2], ***Nicola D'Agostino*** [2], ***Gaetano Festa*** [1,2]

[1] Department of Physics 'Ettore Pancini', University of Napoli Federico II, 80126 Napoli, Italy.

[2] Istituto Nazionale di Geofisica e Vulcanologia, Rome, Italy.

[3] Department of Geophysics, Stanford University, Stanford, CA 94305, USA.

Corresponding author: Francesco Scotto di Uccio (francesco.scottodiuccio@unina.it)

Key Points:

- Accurate earthquake location for enhanced catalogs unveils kilometric scale structures where seismic sequences occur in Southern Apennines.
- Static stress transfer drives the evolution of these seismic sequences, with earthquakes dominantly distributed along the dip direction.
- Slip-dominated alignments of the seismicity could map the fault roughness or the boundary between locked and creeping domains.

Abstract

The use of seismic catalogs enhanced through advanced detection techniques improves the understanding of earthquake processes by illuminating the geometry and mechanics of fault systems. In this study, we performed accurate hypocentral locations, source parameters estimation and stress release modelling from deep catalogs of microseismic sequences nucleating in the complex normal fault system of the Southern Apennines (Italy). The application of advanced location techniques resulted in the relocation of ~ 30% of the earthquakes in the enhanced catalogs, with relocated hypocenters clearly identifying local patches on kilometer-scale structures that feature consistent orientation with the main faults of the area. When mapping the stress change on the fault plane, the inter-event distance compared to the size of the events suggests that the dominant triggering mechanism within the sequences is static stress transfer. The distribution of events is not isotropic but dominantly aligned along the dip direction. These slip-dominated lineations could be associated with striations related to fault roughness and could map the boundary between locked and creeping domains in Apulian platform and basement.

Plain Language Summary

The development of earthquake detection techniques, based on machine learning or similarity, has allowed to increase seismic catalogs of more than one order of magnitude. However, how much information can be extracted from these small cracklings is still to be understood, especially in complex normal fault systems, such as the Apennine environment in Italy. For seismic sequences in Southern Apennines, we show that only a few portion (about 30%) of events in enhanced catalogs can be further characterized in terms of location and source properties. Nevertheless, the use of deep catalogs allows to illuminate kilometric scale structures at depths between 8 and 15 km, to define mechanisms for seismicity evolution, mainly driven by static stress triggering, to identify seismicity alignments along the slip direction, eventually associated with fault roughness or delimiting boundaries between locked and creeping regions.

1 Introduction

Seismic sequences are comprised of earthquakes that are clustered in space and time and that occur at a higher rate than the background seismicity. They contain powerful information for investigating the geometry and mechanical state of faults that may generate large magnitude earthquakes. In the case of a major event, accurate location of foreshocks and aftershocks can inform the rupture process from the preparation phase to the arrest by illuminating the structural complexity of the causative fault (e.g., Lomax 2020, Waldhauser et al. 2021). Most sequences, however, occur during the interseismic period between large earthquakes, at smaller space scales, and feature main events of low to moderate magnitude (Chiaraluce et al. 2009). These sequences can last from few days (Stabile et al. 2012, Scotto di Uccio et al. 2023) to months or years (Kaviris et al. 2021) and can provide insights into stress conditions at depth, potential asperities (Festa et al. 2021), fluid diffusion (Chen et al. 2012), aseismic processes (Gualandi et al. 2017), or other forcing mechanisms that can perturb the stress state in the brittle crust (Silverii et al., 2019).

Knowledge of structures and processes from the analysis of the sequences strongly depends on the content and the magnitude of completeness of available catalogs. Recently, enhanced catalogs obtained through advanced automatic detection techniques such as machine learning and similarity-based approaches (Chamberlain et al. 2018, Zhu & Beroza 2018, Mousavi et al. 2020, Liu et al. 2020, Spallarossa et al. 2021, Scotto di Uccio et al. 2023, Sugan et al. 2023) have contributed to increase the number of newly cataloged events by more than one order of magnitude, improving the magnitude of completeness by at least one magnitude unit. Machine learning based phase pickers have been shown to provide phase arrival times consistent with analyst identifications (Mousavi et al. 2020, Cianetti et al. 2021, Münchmeyer et al. 2022), even for earthquakes outside the regions used in the training datasets (e.g., Mousavi et al. 2020, Park et al. 2020, Tan et al. 2021). Furthermore, event similarity can be exploited for closely spaced events using cross-correlation to measure P and S arrivals for smaller magnitude earthquakes from template events (Poupinet et al. 1984, Vuan et al. 2018, Chamberlain et al. 2018).

Phase picks can be used for precise earthquake location using differential location methods (Waldhauser & Ellsworth 2000, Trugman & Shearer 2017). However, hypocenter determination of low magnitude earthquakes in enhanced catalogs is challenging because these events typically emerge from the noise only at the few closest stations with uncertain arrival times. A typical percentage of template matched events that can be relatively located from enhanced catalogs is ~ 20% (Cabrera et al. 2022). Nevertheless, accurate locations from deep catalogs can provide a high-resolution image of fault structures, help to discern their interaction (e.g., Ross et al. 2019, Park et al. 2022, Sugan et al. 2023), and illuminate paths for possible fluid migration (Ross et al. 2020, Vuan et al. 2020).

Deep catalogs can be statistically exploited in their space-time-magnitude evolution for inferring macroscopic physical processes to relate seismic sequences to background seismicity (Hermann et al. 2022, Scotto di Uccio et al. 2023), which may improve the predictability of short-term forecasting (Gulia & Wiemer 2019, Beroza et al. 2021). Reliable estimation of the frequency-magnitude characteristics of the catalogs requires a correct estimation of the event size and the catalog magnitude of completeness to avoid biases in b-value estimates (Marzocchi et al. 2020, Mancini et al. 2022).

Extracting physical constraints on the source process of events in deep catalogs is challenging due to the small signal-to-noise ratio and the narrow available frequency band. Local and moment magnitudes for small events can be estimated using time or frequency domain measurements (e.g., Abercrombie 1995, Edwards et al. 2015, Hawthorne & Burtlow 2018, Supino et al. 2020, Scotto di Uccio et al. 2023). The source corner frequency (or event duration in time domain), which is a proxy for the earthquake size, can be obscured by anelastic attenuation effects (Deichmann, 2017) or the sampling rate (Abercrombie 2015). Several approaches have been proposed to reduce the correlation between the attenuation of the medium crossed by seismic waves and the source parameters. These are either based on the Empirical Green's function (EGFs) approach (Mori & Frankel 1990, Prieto et al. 2004), or based on the determination of attenuation relationships (Oth et al. 2007), which can allow a decrease in the minimum magnitude for which the source parameters can be estimated (Abercrombie 2015). While the use of EGFs is appealing in removing the propagation contribution, small events should be at least one point of magnitude smaller than the earthquake for most EGF approaches (Abercrombie & Rice 2005). EGF availability is often limited at the stations closest to the hypocenter, in a limited frequency band, where the signal emerges from the noise. When properly retrieving the source parameters for events in the sequence, they can help constrain the mechanisms associated with their evolution, e.g., whether they are triggered by stress release in cascade-like models or are driven by other forcing mechanisms (e.g, Stabile et al. 2012, Yoon et al. 2019).

In this study we focused on seismic sequences in the Irpinia region, Southern Apennines (Italy). The area is one of the highest hazard regions of Italy (Stucchi et al. 2011) and experienced the most destructive seismic event in recent decades in that country. The 1980, M 6.9, Irpinia earthquake occurred on multiple, separate fault segments that were activated within 40s of the event origin (Figure 1), leading to more than 3000 casualties (Rovida et al. 2019). The region is currently deforming, with a strain rate of ~100 nstrain/yr corresponding to an increase of ~3 mm/yr over 30 km across the axis of the Apennines (Daout et al., 2003; Figure 1). In the last 15 years, the area has been monitored by the Irpinia Near-Fault Observatory (INFO, triangles in Figure 1), with a dense seismic network of 31 stations equipped with accelerometers and short-period or broad-band seismometers (Iannaccone et al. 2010, Chiaraluce et al. 2022). Recent seismicity is characterized by low magnitude events (maximum magnitude 3.8), mainly occurring at depths between 8 and 15 km (De Landro et al. 2015), within the fault system that generated the 1980 Irpinia earthquake and is mainly concentrated in a volume of low vs, high Qp, high vp/vs, which suggests fluid-saturated conditions (Vassallo et al. 2016, Amoroso et al. 2017). Also, source parameters show a variability in the stress drop that could be modulated by fluid composition and concentration (Picozzi et al. 2021). In the area seismicity sometimes occurs clustered in seismic sequences that last several days, characterized by main events of magnitude lower than 3.5. Detailed studies of two sequences have shown a complex pattern for the seismicity and suggested that stress triggering can be the main driver of their evolution (Stabile et al. 2012, Festa et al. 2021). Recently an enhanced catalog for 10 seismic sequences has been obtained for the area (Scotto di Uccio et al. 2023), built on the integration of machine learning and template matching, that increased the number of events relative to the existing manual catalog by a factor 7. In this study we seek to exploit the improved catalog to better understand the space-time evolution of the seismic sequences. We found that seismic sequences can be accurately located with uncertainties of ~100 m, they occur on secondary structures with respect to the main segments of the 1980 Irpinia earthquakes and their evolution appears to be mainly driven by static stress transfer. Preferential alignments of the seismicity along the dip direction might be an indication of simultaneous aseismic transients, especially for the most populated sequence.

First, we present the data used in the work (Section 2). Then, we describe the methods for accurately locating the events in the sequence, determining the source parameters and building a model to describe the stress release on the fault plane hosting the sequence (Section 3). Finally, we present the results obtained for the sequences, interpreting their spatio-temporal evolution (Section 4), along with discussions and conclusions.

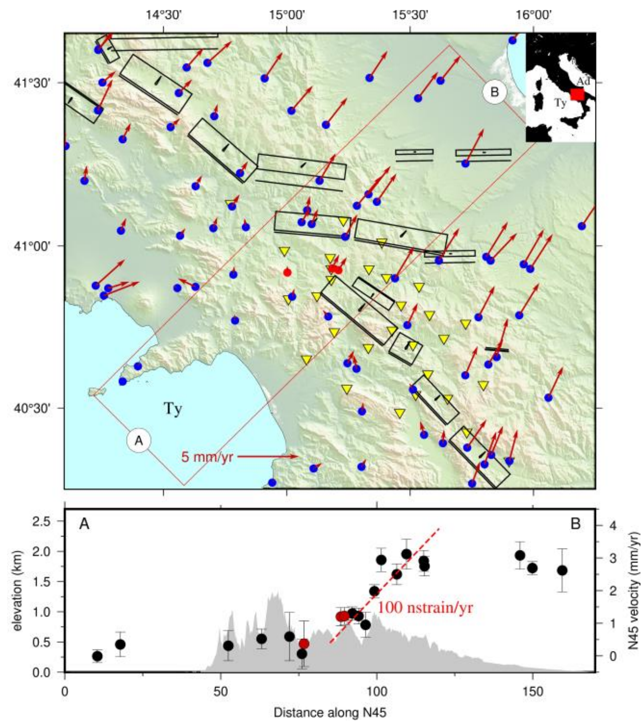

Figure 1) Top panel: GPS velocity field in a Tyrrhenian reference frame. Yellow triangles indicate the seismic stations of INFO. GPS stations SNAL, ANG1, and MTMR are displayed in red circles. The black boxes are the historical faults that generated the largest earthquakes in the area, as reported by the Database of Individual Seismogenetic Sources (DISS, https://seismofaults.eu/services/diss-services). Bottom panel: Elevation along the A-B section of top panel and velocity field related to the GPS stations within the red box of top panel along the N45E direction. The study area is currently accumulating strain at ~100 nstrain/yr corresponding to an increase of ~3 mm/yr across the axial part of the Apennines.

2 Data

In this work we characterized the spatio-temporal evolution of seismic sequences that occurred near the Irpinia Near Fault Observatory. The sequences occurred between 2011 and 2020 and featured main events of low to moderate local magnitude (1.8 < Ml < 3.7). We selected the enhanced catalogs obtained by Scotto di Uccio et al. (2023) using machine learning derived detections (EQTransformer, Mousavi et al. 2020) as template sets for a further similarity-based detection (EQCorrscan, Chamberlain et al. 2018). The integration of machine learning and template matching has been shown to improve the manual catalogs by a factor ~7 in this region. The catalogs for the sequences obtained in Scotto di Uccio et al. (2023) feature an improved magnitude of completeness of more than one magnitude unit and provide ~1.8k events, with nearly 800 events in the Rocca San Felice sequence.

We extended the initial phase-pick dataset to all the stations not included in the detection step in Scotto di Uccio et al. (2023). We used the velocity data when available, and the acceleration data as a second choice, following the same strategy used in Scotto di Uccio et al. (2023).

The cross-correlation delay times for double difference earthquake re-locations were evaluated on traces decimated to 100 Hz (Michele et al., 2020), obtained trimming raw continuous waveforms around the origin time from absolute locations. In the evaluation of source parameters for the relocated events, we pre-processed the raw traces by removing the instrumental response, including a 5% Hann taper and a water level regularization during the deconvolution stage. We bracketed the *S* wave window from 1 s before to 3 s after the phase arrival time. We considered the frequency band that satisfied the condition of SNR between the event and the noise spectra larger than 3.5 based on a comparison with a 4s time window before the event origin time.

3 Methods

3.1 Absolute and relative locations

For locating the earthquakes in the enhanced catalogs, we used available P and S arrival times. For template events, we obtained phase arrival times with the machine learning picker. The consistency between the automatic and manual picks was demonstrated in Scotto di Uccio et al. (2023), who found that the residuals featured zero mean values and a slightly larger dispersion for the S phase (standard deviation of 0.2 s). For the low magnitude events identified by the template matching, they performed cross-correlation (CC) picking and retained those measurements with a CC value of greater than 0.7. The consistency of template picks helps to ensure the reliability of the CC-derived phase arrival times. Moreover, the similarity-based detection step can add missed picks by machine learning picker, also for events with moderate signal-to-noise ratio (Park et al. 2023). When an arrival time was declared by both pickers, we selected the phase provided by the machine learning technique. Arrival time uncertainties are estimated by considering the associated probability for machine learning picks and the CC values for template matching phases, respectively. We converted the probability values (ranging between 0.1 and 1.0) into discrete weights for location (from 0 to 4, increasing numbers correspond to larger uncertainties) according to the table proposed by Mousavi et al. (2020). For the template matching picks, we imposed at least the same level of accuracy of the machine learning picks used for the declaration, eventually increasing the discrete weights for low cross-correlation values. We raised the discrete weights by one point for every decimal of CC coefficient detaching from 1.0.

We estimated earthquake location using NonLinLoc (Lomax et al. 2000), which adopts a probabilistic approach to determine the location using the travel time residuals with statistically robust uncertainties. We tested three velocity models for the location procedure. Starting from a 1-D layered velocity model tailored for the Irpinia area (Matrullo et al. 2013), we derived two gradient models, which smooth the discontinuities in the wave velocity across layer boundaries, by linearly interpolating values between either the top or the middle points of the layers (Figure S1). We note that the velocity model obtained fixing the velocity value at the top of the layers systematically overestimates the velocity in each layer. The interpolated model obtained by fixing the velocity values at the centre of the layers resulted in lower location uncertainties, so we selected this model for event location. A few poorly constrained events result in an unreliable shallow location estimate; for these cases, we selected the location solutions obtained from the expected values of the probability density function (Lomax et al. 2000).

We used absolute locations as the starting point for relative re-locations of events in each sequence using HYPODD (Waldhauser & Ellsworth 2000), based on differential travel times for event pairs. For the evaluation of the catalog delay times in each sequence we used the picks for event pairs separated by less than 10 km in absolute location at all the available stations. For CC differential travel times, we evaluated the delay times for events that were separated by less than 10 km, on seismograms decimated to 100 Hz and filtered in the frequency band [1.5 – 15] Hz (Schaff et al. 2004, Michele et al. 2020).

We assessed the length of the time windows for extracting the waveforms around the P and S arrival times by performing parametric tests. Too short windows resulted into too high values of CC coefficients such that he reliability of the lag measurement was overestimated. We selected a 1.1 s (1.4 s) long window around the P (S) phase arrival time for calculating the CC coefficients, imposing a maximum lag of 1s. We only retained delay times for events with CC coefficient higher than 0.7.

We estimated relative locations with HYPODD using an iterative least square procedure (LSQR) that minimized the differential time residuals for pairs of earthquakes recorded at common stations by adjusting the vector connecting their hypocentres (Waldhauser & Ellsworth 2000). We used 4 steps of 4 iterations (a total of 16 iterations) of damped and dynamically weighted least square inversions. In the initial settings, we assigned higher weights to catalog delay times, for better constraining the location of the clusters, and we increased the contribution of the CC differential travel times in the following settings, to consider the different position of the events within the cluster. The damping factor was selected to stabilize the problem (Waldhauser 2001). To avoid inconsistency with ray patterns used in the absolute locations, we extracted a 1-D model composed of 20 thin layers from a resampling of the velocity model used in the absolute locations.

LSQR only approximates some aspects of the uncertainty (Waldhauser & Ellsworth 2000), so we applied the Singular Value Decomposition (SVD) method for a more complete assessment of location errors. The SVD option for double difference locations can only solve for a significantly lower number of earthquakes than the LSQR option. Nevertheless, we were able to apply the SVD technique for all the sequences apart from the Rocca San Felice sequence. For this latter sequence, discussed in detail in the Section 4, we estimated location uncertainties using a bootstrap strategy. We realized 200 independent double difference location runs on subsets of events within the sequence. Each subset was obtained by randomly extracting 150 events, 60 % of which belong to the machine learning catalog. This constraint in the selection of the events in each subset ensures a more robust linkage to the cluster, since the number of picks associated with templates is generally larger than for template-matched events. We evaluated the location uncertainties from a statistical analysis based on the distance of each event from the cluster centroid for all the runs where that event was located. This procedure allows quantification of the dependency of the results on the single subset. For the $i-\mathrm{th}$ event we estimated the uncertainty along the $j-th$ direction as $err_j^i = median_{(p,m)}|(x_{j,p}^i - x_{j,p}^c) - (x_{j,m}^i - x_{j,m}^c)|$, where p and m indicate two independent runs in which the $i-\mathrm{th}$ event was located, and the superscript c refers to the cluster centroid of the considered run. The robustness of these estimates has been verified observing agreement with uncertainties from a SVD inversion for the subset of template events.

3.2 Source Parameters

We used a probabilistic inversion approach (Supino at al., 2019) for retrieving earthquake source parameters (seismic moment M_0 and corner frequency f_c) from the S-wave displacement amplitude spectra of relocated events. This technique is grounded in a Bayesian inversion of the spectra and allows an exploration of the correlations among parameters with a robust estimation of the uncertainties. The source is described by a generalized Brune model (Brune, 1970)

$$\tilde{S}(M_0, f_c, \gamma; f) = \frac{M_0}{1 + \left(\frac{f}{f_c}\right)^{\gamma}} \tag{1}$$

where the spectral fall-off at high-frequencies γ is considered as free parameter. The propagation contribution is described by the term (e.g., Supino et al. 2019)

$$\tilde{G}(Q, f) = KAe^{-\pi f T/Q} \tag{2}$$

where T is the source-receiver travel-time, Q is the quality factor related to anelastic attenuation, A is the geometrical spreading (assumed as $1/r$, where r is the source-receiver distance) and

$$K = \frac{R_S F}{4\pi\rho\beta^3} \tag{3}$$

We assumed the average radiation pattern for S-waves $R_S = 0.63$ (Boore & Boatwright 1984), a free surface reflection coefficient of $F = 2$, the density $\rho = 2700\ kg/\mathrm{m}^3$ and the S-wave velocity $\beta = 3027\ \mathrm{m/s}$ (Zollo et al. 2014). After removing the instrumental response, the displacement amplitude spectrum can be written as:

$$\tilde{U}(M_0, f_c, \gamma, Q; f) = \tilde{S}(M_0, f_c, \gamma; f) \cdot \tilde{G}(Q; f) \tag{4}$$

The modelling of the spectra requires a joint inversion for source parameters and quality factor, which are strongly correlated. To reduce this correlation, we tried to evaluate the quality factor separately from the inversion of source parameters. We started by considering the small events in each sequence as empirical Green's functions (EGF). For those events the effective (source) corner frequency is much larger than the apparent corner frequency of the anelastic attenuation low-pass filter, and sometimes even larger than the Nyquist frequency of the records (in this case $f_{Nyq} = 62.5$ Hz). Considering the EGF spectra in the domain where $f \ll f_c$, the displacement spectrum can be approximated as:

$$\tilde{U}_{EGF} = KAM_0\, e^{-\pi f T/Q_{EGF}} \tag{5}$$

We selected events featuring local magnitude $Ml < 1$ as EGFs and fit with a linear model $\log\tilde{U}_{EGF}$ as a function of the frequency to retrieve M_0 and Q_{EGF}. The frequency band selected for the fit respects the constraint of a signal-to-noise ratio larger than 3.5 for each frequency in the band. The value of Q_{EGF} is station dependent.

Since events in the same sequence share almost the same source-receiver path, we expect a consistency in the Q_{EGF} estimates across the EGFs for the same station. For stations presenting at least 5 estimates of Q_{EGF}, we evaluated the compatibility of the inferred values and used the mean value to correct for anelastic attenuation.

For other stations, for which we have insufficient high-quality EGFs, we attempted to estimate a sequence-dependent quality factor Q_{LOC} by exploring different values of the anelastic attenuation around the average regional estimate $Q_{REG} = 230$ (Zollo et al., 2014). Considering events with $Ml > 1$, we inverted the displacement amplitude spectra, and fixed the attenuation to one of the following values $Q = 100, 170, 230, 300, 400$ in different inversion runs. We compared the average residuals resulting from the best solution for the source parameters in each run. We selected as Q_{LOC} the Q value producing the lowest misfit, imposing a minimum number of 5 solutions per station. We finally kept $Q = Q_{REG}$ for stations where neither Q_{EGF} nor Q_{LOC} could be evaluated.

Finally, the inversion technique provided the seismic moment M_0 (and the moment magnitude M_w) for all the events, but corner frequencies only for events with $Ml > 1$. Quality of the solutions was checked by analysing the shape of the a-posteriori probability density function related to the estimated parameters. Solutions not showing peaked probability functions were discarded following the strategy defined in Supino et al. (2019).

3.3 Stress change model

For events in the sequence for which we estimated both moment magnitude and corner frequency, we computed the source radius a as (Madariaga, 1976):

$$a = k\frac{\beta}{f_c} \tag{6}$$

where k is a geometrical shape factor, which was assumed here as $k = 0.37$ (Brune, 1970). We derived the stress drop $\Delta\sigma$ from seismic moment and the source radius (Keilis-Borok 1959) as:

$$\Delta\sigma = \frac{7}{16}\frac{M_0}{a^3} \tag{7}$$

We then evaluated the average stress drop $\Delta\bar{\sigma}$ for the sequence as the mean value of the retrieved stress drops. We associated the average stress drop $\Delta\bar{\sigma}$ with all other events in the sequence for which we were not able to estimate the corner frequency, and we used the above relationship to retrieve the event source radius.

We evaluated the rupture plane associated with the seismic sequence as the best-fit plane across the hypocenters of the events in the sequence. If the locations did not constrain a plane, we used the focal mechanism solutions from Palo et al. (2023) and selected the plane that is more consistent with the expected orientation of faults in the area. We finally mapped the stress change on the fault plane associated with the sequence, using the rupture model proposed by Andrews (1980) and a non-isotropic representation of the stiffness. Since in the rupture model neither the slip nor the stress drop is considered constant, we imposed the condition that the average stress drop within the crack from the Andrews model coincided with the event stress drop computed from the source parameters.

4 Results

For all the enhanced catalogs related to the sequences in Scotto di Uccio et al. (2023), we computed absolute and (double difference) relative locations using NonLinLoc and HYPODD codes. Using the automatic phase arrival times provided by the integration of machine learning and template matching pickers, we obtained absolute locations for 1130 events (~60 % of the detection catalog). The uncertainties can be as large as few kilometers, resulting into several tenths of second root-mean square (RMS) of travel time residuals. This uncertainty is enough to obscure the fault segments or patches on which the seismicity takes place. The number of absolute locations from the enhanced catalogs is 5 times larger than in the manual INFO bulletin and provides a wide set of catalog and cross-correlation delay times for earthquake relocation. When analyzing the single sequences, the improvement in the number of located earthquakes ranges from a factor 2.5 to 8.5.

Starting from the absolute positions of earthquakes in the enhanced catalogs, we achieved double difference relocation of 550 events total, from 8 out of the 10 seismic sequences analyzed in Scotto di Uccio et al. (2023). The two sequences for which we did not get relocations (IDX 7 and IDX 9 in Scotto di Uccio et al. 2023) feature the lowest number of detections (about 40 events). The total number of relocated events represents ~ 30% of the enhanced catalog. A similar fraction is observed for each of the relocated sequences and results coherent with earthquake relocation of other template matching derived catalogs (Cabrera et al. 2022, Ross et al. 2019), due to low signal-to-noise ratio of small events leading to limited pick availability and triggered stations.

Figure 2 shows the double difference relocation of the earthquakes in the enhanced catalogs. In the left panel we show the position of epicenters with respect to the seismic network. In the right panel the hypocenters are projected along the vertical plane A-A' oriented perpendicular to the trend of the Apennines (N40°E). This plane represents the direction orthogonal to the main structures of the area, that generated the 1980 Irpinia earthquake. In Table S1 we report the label of the sequences in this work with respect to the references in Scotto di Uccio et al. (2023).

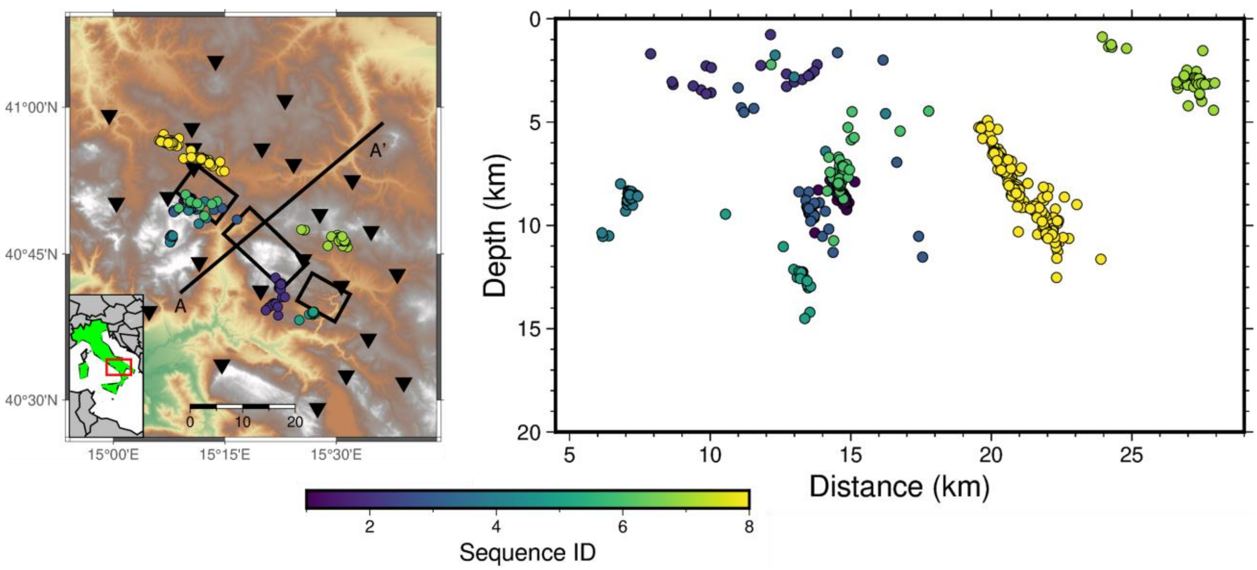

Figure 2) Left panel: Epicentral location for the relocated events, colored according to the sequence IDX and representation of the fault traces in the Irpinia area. Stations are shown with black triangles. Right panel: Cross-section along the A-A' vertical plane, orthogonal to the main structure of the 1980 M 6.9 earthquake for which rupture planes are shown with black rectangles.

The cross-section shows that the seismicity patterns feature clear alignments and a high degree of clustering, highlighting km-sized structures that share similar dips. For all sequences, the spatial extent of the sequences depicted by relocations is much greater than what expected from the total released seismic moment.

The Rocca San Felice sequence, marked in Figure 2 with yellow dots (IDX 8) features the highest number of both detections and double difference located events (~800 and 250 events respectively). For this sequence, we were able to estimate absolute locations for about 60 % of the detections, with average horizontal and depth uncertainties of 1.5 km (average RMS residuals of 0.4 s). We evaluated double difference relocations, limiting the analysis to events with at least 2 P-picks and one S-pick among the three stations closest to the centroid of the sequence (~300 located earthquakes). From about 97.5 k catalog differential times (47k for P phase, 50.5k for S phase) and 85k CC delay times (31k for P phase, 54k for S phase) we obtained a catalog of 250 relocated events with median location uncertainties of 91 m, 31 m and 105 m in the East, North and vertical directions, respectively. When zooming on the sequence location (Figure 3 - left panel), the position of the epicenters clearly suggests the presence of two clusters, at 5 km of distance from each other. The projection of the seismicity along the vertical plane oriented N40°E (Figure 3 – right panel), indicates that the two clusters feature similar orientations but occurred at different depths: the shallower one is mostly confined between 6 km and 9 km, the deeper one between 9.5 km and 11 km. The two clusters were activated at different times during the sequence, as shown in Figure 3, where the colors denote the occurrence time of the events relative to the mainshock. The events occurred within the first two days of the mainshock illuminate a first 4-km long segment with a dip of 55°, coherently with the focal mechanism estimated by Festa et al. (2021). Two days after the main event, the occurrence of a Ml 2.8 event activated a deeper secondary patch of slightly shorter extent with a similar orientation.

The presence of two separated clusters was not recognized in the previous work of Festa et al. (2021) and is supported by the change in the first station recording the P wave arrival, that occurred at the station RSF3 for events in the first cluster and at LIO3 for events in the second one. In Figure S2 we reported the vertical records, at the closest stations, for two events belonging to the two clusters. It is worth to note that the improvement in double difference location as compared to the results of Festa et al. (2021) comes from the combination of a deeper event catalog, but also from a larger number of picks per event. Indeed, for most of the events we were able to retrieve picks and waveforms also for the accelerometric station SALI, located close to the centroid epicenter, indicating that strong motion sensors can provide useful information even for microseismic events if their sensitivity is high enough (for SALI it is 4.0 $V/m/s^2$).

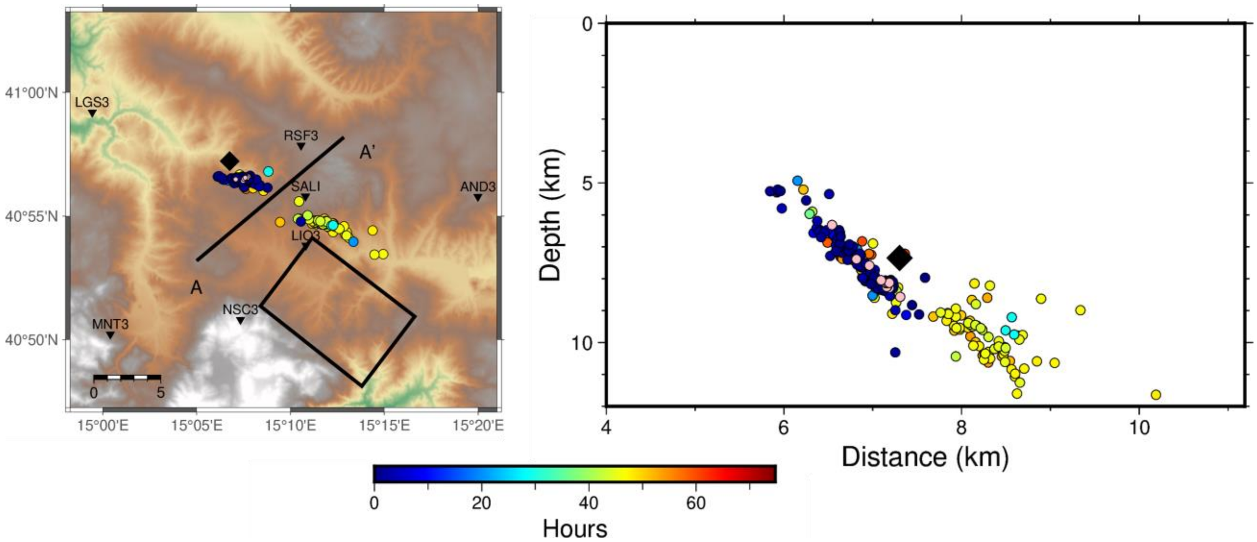

Figure 3) Left panel: Spatio-temporal evolution of the epicenters for the Rocca San Felice seismic sequence (IDX 8), colored according to the occurrence time from the main event. Foreshocks are represented with pink circles and the main event is represented with a black diamond. Right panel: Cross-section along the vertical plane as in Figure 2, colored according to the occurrence time from the main event.

We inverted the displacement spectra of the relocated events to infer the seismic moment M_0 (and hence the moment magnitude M_w), the corner frequency f_c and the quality factor Q as output. For each sequence, we separated events with local magnitude above and below 1.0, according to the estimates of Scotto di Uccio et al. (2023) as described in Section 2. We then estimated M_0 and Q for the events in the sequence below the magnitude threshold, considered as EGFs, and used these parameters to infer the moment and the corner frequency of the larger events (above the threshold).

Here, we illustrate all the steps in our analysis for the Rocca San Felice sequence, which we also applied to all the other sequences. For the stations closest to the sequence, recording many small magnitude events ($M_l < 1$), we tried to estimate the quality factor Q_{EGF} by fitting the logarithm of the displacement spectra as a linear function of the frequency. For each EGF, we perform the fit in the frequency band where the signal-to-noise ratio exceeds the threshold of 3.5. As an example, we show in Figure 4 - left panel- the displacement amplitude spectrum and the corresponding noise spectrum for a M_l 0.41 ± 0.10 earthquake at the station NSC3 ($\sim$ 11 km distance from the main event). We estimated the quality factor for the considered earthquake from the slope of the linear fit (Figure 4, left panel), whose intercept is proportional to the seismic moment. We thus estimated the quality factor Q_{EGF} from the fit of each candidate EGF. An example of Q_{EGF} distribution (for the station NSC3) is reported in the right panel of Figure 4. We observe a peaked Gaussian-like distribution, which is typical of stations providing a large number of estimates for the quality factor. We extracted the weighted mean of individual Q_{EGF} values using the inverse of the fit residuals as weighting factors, to describe the quality factor $\bar{Q}_{EGF}$ for that station-sequence couple.

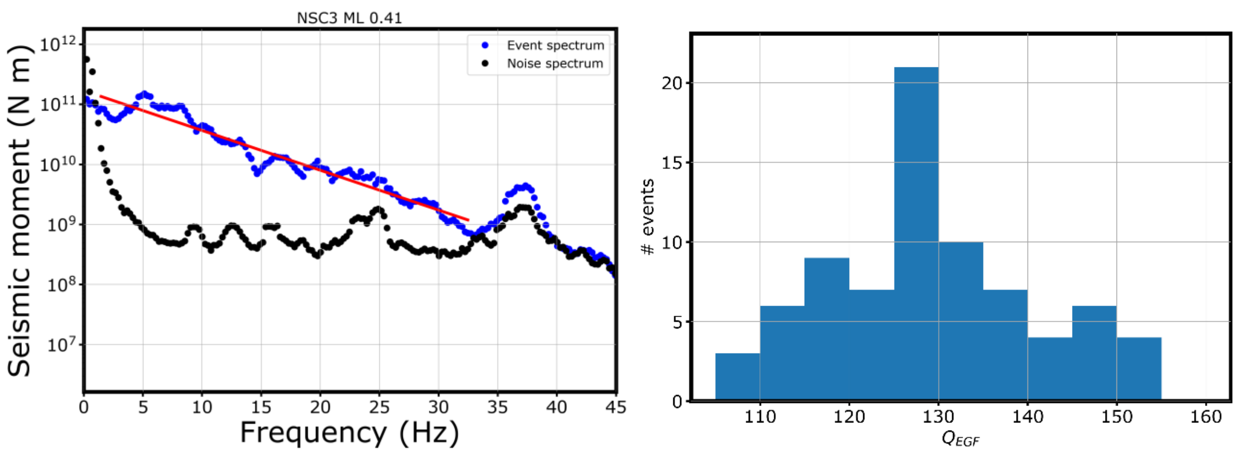

Figure 4) Left panel: Q_{EGF} estimation from linear fit (red solid line) of the logarithm of the displacement event spectrum (blue dots) as a function of the linear frequency, for a $M_l = 0.41$ earthquake. Noise spectrum is reported as black dots. Right panel: histogram of the Q_{EGF} for the events M_l < 1 in the Rocca San Felice sequence (IDX 8) at NSC3 station

For the example of Figure 4, we estimated $\bar{Q}_{EGF} = 130 \pm 12$ for NSC3, which is smaller than the regional estimation provided by Zollo et al. (2014).

For the stations lacking sufficient high-quality EGFs, we attempted to extract a local quality factor Q_{LOC} by performing several inversions with different, fixed Q_s values. We then assumed as the most suitable value of Q the one that resulted in the lowest average RMS residuals. In the case of the Rocca San Felice sequence, this procedure allowed estimation of the quality factor for five stations (COL3, SCL3, SFL3, SNR3, SSB3). For stations where neither Q_{EGF} nor Q_{LOC} was estimated, we considered the regional value of the area for the quality factor ($Q_s = 230$, Zollo et al. 2014). After the estimation of the quality factor from the EGF, we attempted to estimate the source parameters for events with $M_l > 1$, by fitting the spectra with the generalized Brune model. In Figure S3 we report the fit results for a M_l = 2.8 event at three stations. In Figure S3 – left panel – we represent the fit of the displacement spectrum at the station NSC3, where we used an EGF derived quality factor ($Q_{EGF} = 130$). In the central panel we report the results for the station SCL3 ($\sim$ 43 km from the main event) where we estimated a quality factor $Q_{LOC} = 300$, higher than the average estimate for the area. We note that in this latter case, the average value ($Q = 230$) provides unreliably large corner frequencies (as compared to the values obtained at other stations), close to the upper limit of the frequency band used for the inversion. In the right panel, we show the fit for the station VDS3 ($\sim$ 38 km from the main event), for which we used the regional value $Q_{REG} = 230$.

For the Rocca San Felice seismic sequence, we retrieved the seismic moment M_0 for 45 % of the located events, while we globally estimated the seismic moment for 236 out of the 550 relocated events (~60%). In Figure 5 - left panel we report the distribution of the moment magnitude M_w (Hanks and Kanamori, 1979), against the local magnitude M_l, as evaluated in Scotto di Uccio et al. (2023), considering all the events for which an estimation of the seismic moment was available. The red line marks the 1:1 trend between M_l and M_w.

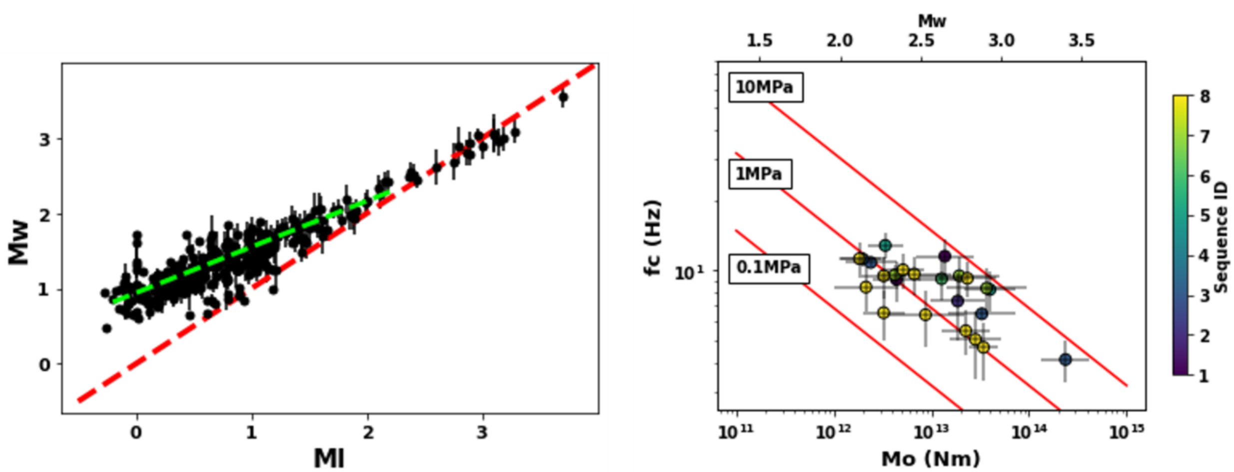

Figure 5) Left panel: M_w - M_l distribution, with the 1:1 relation scaling reported as dashed red line. For $M_l < 2$ earthquakes, we observed $M_w = 0.89\ (\pm 0.03) + 0.62\ (\pm 0.02) M_l$ (green dashed line). Right panel: Distribution of source parameters for $M_w > 2$, colored according to sequence IDX, with theoretical constant stress drops scaling of 0.1 MPa, 1 MPa and 10 MPa (red solid lines)

We recognize two trends between the magnitude scales: for $M_l < 2$ the distribution strongly deviates from the 1:1 scaling relation. Evaluating the average value of M_w in different M_l bins of width 0.2 and performing a linear fit between the two quantities, we retrieved $M_w = a + b * M_l = 0.89\ (\pm 0.03) +\ 0.62\ (\pm 0.02) M_l$ (the linear fit curve is reported with a green dashed line). The estimated slope agrees with the predictions of Deichmann (2017), which indicated a saturation of the event duration in the local magnitude computation due to the anelastic attenuation, resulting into the scaling $M_w = C + \frac{2}{3} M_l$. For $M_l > 2$, the distribution follows the 1:1 scaling trend between M_l and M_w, as also found by Zollo et al. (2014). In the right panel of Figure 5 we reported the $\log M_0 - \log f_c$ distribution, with red straight lines marking the theoretical trends obtained assuming characteristic stress drop values of $\Delta\sigma = 100kPa, 1MPa$ and $10\ MPa$. The single station corner frequencies have been averaged considering the relative uncertainty of the estimate. As a result, we determined seismic moment and corner frequency for events with moment magnitude $M_w > 2.0$, while for events below this magnitude, the solution for the corner frequency was not constrained (Supino et al. 2019). For the resolved events, the distribution of the corner frequencies with moment appears to follow a nearly linear trend, with stress drop ranging between 1-3 MPa. For the Rocca San Felice sequence, yellow marks in the right panel of Figure 5, the average $\Delta\sigma$ resulted to be $\sim 1.0\ MPa$

We evaluated the source size for all the events for which we estimated the seismic moment, either by considering the retrieved corner frequency or by assuming self-similarity. The former condition applies to the largest magnitude events in the sequences, the latter for lower magnitude events. For each sequence, we assessed the best fitting plane from earthquake locations, and represented the static stress released by single events onto this plane (Andrews et al. 1980) along the strike and dip directions. For almost all the sequences (IDXs 1 to 7) the stress model suggests static stress release as a trigger mechanism, with small events mainly concentrated in or around the area affected by stress changes due to the main events in the sequence. As an example, we report in Figure 6 – left panel - the stress release model for a seismic sequence featuring a M_l 2.9 main event (IDX 1 in Figure 2). We observe a single km-sized patch mainly oriented along the dip direction, with earthquakes occurring within the volume interested by the main event. We retrieved similar dip – oriented trends also for the other considered sequences. An interesting case is represented by the Rocca San Felice seismic sequence (IDX 8 in Figure 2 and in Figure 3), illustrated in the right panel of Figure 6. For this sequence, we observe two seismicity patterns activated at different times (the main event M_l 3.0 involved the leftmost patch, and the seismicity migrated along the rightmost segment almost two days after the mainshock with the occurrence of a M_l 2.8 earthquake). In both clusters we still observe a predominant orientation along the dip direction. In the following discussion, we investigate the mechanical connection between these two patches.

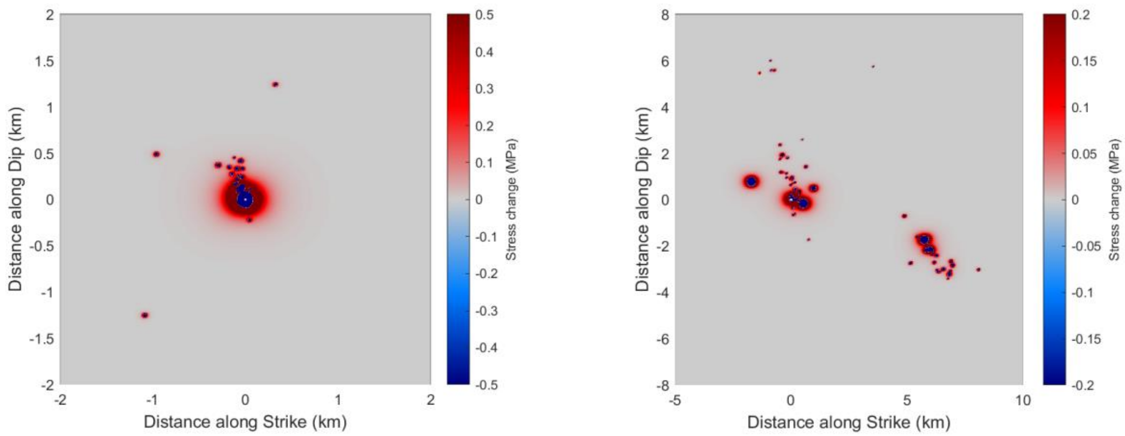

Figure 6) Stress released model for the IDX 1 (left panel) and IDX 8 (Rocca San Felice, right panel) sequence. In both representations, we observe earthquakes occurring within the volume interested by the main event, with preferentially dip-oriented patches.

5 Discussion

Catalog enhancement using advanced detection techniques allows an increase in the number of earthquakes up to an order of magnitude as compared to ordinary seismic catalogs. For seismic sequences in the normal fault system of Southern Apennines (Italy), we find an enhancement of a factor ~ 7 with respect to the number of earthquakes manually detected by network operators (Scotto di Uccio et al. 2023). The improvement in the magnitude of completeness of these deep catalogs makes it possible to monitor variations in the statistical parameters describing the seismicity, such as the b-value of the Gutenberg-Richter relation (Beroza et al. 2021). These changes can only be roughly indicative of variations in the mechanical properties underlying the faults, such as the differential stress (Scholz 2015); however, the evaluation and the consequent use of these parameters for interpreting the evolution of the sequences is still debated, in part due to biases in the magnitude estimates (Gulia & Wiemer 2019, Hermann & Marzocchi 2021, Mancini et al. 2022).

The clearer view of the manifestation of the mechanical properties of structures in the form of earthquake sequences can be achieved through accurate location and source parameter estimation; however, the generally low signal-to-noise ratio of the new events in the enhanced catalogs, does not fully translate into an equal increase in the number of earthquakes that can be accurately located. For seismic sequences in Irpinia, we retrieved double difference locations for $\sim 30\ \%$ events, a fraction similar or slightly larger than the percentage resulting from template matching derived catalogs (Ross et al. 2019, Simon et al. 2021, Cabrera et al. 2022). This reduction in the number of well-located events is driven by the different impact of the waveform similarity during the detection and the location phases. Template matching detection algorithms leverage on stacked cross-correlations across the entire network (Chamberlain et al. 2018, Vuan et al. 2018), resulting in a global similarity value, to which stations with both high and low cross-correlation values contribute. High-quality thresholds on the similarity coefficient for cross-correlation differential travel times requested by accurate double difference locations (Michele et al. 2020, Waldhauser et al. 2021), limit the number of available stations, especially for low magnitude events. Although the catalog of events located with double differences is only twice larger than the manual catalog, the improvement in cluster definition and spatial resolution is much more significant, allowing the identification of alignments and structures at kilometric scale, that were not clearly illuminated from the manual catalog (Palo et al. 2023), owing to the wide increase in the number of differential travel-times. As an example, for the Rocca San Felice sequence, we reported more than one order of magnitude more differential travel-times compared to the ones extracted from the manual catalog (Festa et al. 2021).

When moving to the moment magnitude estimation, the number of events in the enhanced catalog that can be characterized further decreases, to 15% of the detections (or 60% of the relocated events). Furthermore, we resolved the corner frequencies only for events with moment magnitude $M_w > 2.0$ already present in the network catalog due to the limited available frequency bandwidth for the inversion related to the signal-to-noise ratio and data sampling rate. Nevertheless, we were able to reduce the epistemic uncertainty in the estimate of source parameters due to the propagation, using small earthquakes as empirical Green's functions.

Averaging over all sequences, we found an average stress drop of $\Delta\sigma = 2.35\ MPa$; its variability across sequences, estimated by the standard deviation is $s_{\Delta\sigma} = 0.87\ MPa$. The stress drop found here is one order of magnitude larger than the stress drop retrieved for the background seismicity in the area by Zollo et al. (2014), who used a similar inversion strategy and an independent catalog not influenced by the sequences studied here. Since they derived the average stress drop using the

Madariaga model (Madariaga 1976), when converting that value into an equivalent Brune's stress drop, they obtained a median value of $\Delta\sigma = 0.26\ MPa$. This difference indicates that the release of stress during sequences likely occurs in more compact asperities that can be associated with a higher coupling than for background seismicity (Chen & Shearer 2012).

The stress drops we retrieved for these seismic sequences are comparable to the estimate of $3.5 MPa$, achieved for the 1980, M 6.9 Irpinia earthquake (Deschamps & King 1983, Bernard & Zollo 1989). When mapping the seismic sequences at depth, their location is generally not compatible with faults that hosted the 1980 event - based on either the fault trace at the surface (Westaway & Jackson 1987) or the event dip and geometry estimated from seismic and levelling data (Bernard and Zollo 1989, Amoruso et al. 2005). This indicates that seismic sequences ruptured small patches of secondary segments, as compared to the main structure of the M 6.9 earthquake.

The investigated area undergoes a strain-rate of ~100 nstrain/yr and an increase of 3 mm/yr over 30 km along the axial sector of the Apennines. All the investigated sequences fall within the actively deforming area, providing important insight into the geometry of structures potentially activated during larger magnitude events. The Rocca San Felice sequence, roughly aligned along the northwestward continuation of the complex multi-segment fault system activated during the M 6.9 earthquake, illuminates a NE-dipping structure whose geometry is favorably oriented for seismic release of NE-SW accumulated interseismic strain (Figure 1). This structure is not mapped in the catalog of the Italian seismogenic Faults (DISS, https://diss.ingv.it/), which should motivate additional investigation of the long-term, seismogenic behavior of the structures illuminated by local seismic sequences.

We found differences in the stress drops associated with sequences, with an increase of the stress drop moving from North to South in the Irpinia region, as also shown by Picozzi et al. (2022), whose catalog contains all the events with magnitude larger than 1.5 for the area. We found average stress drops of $\Delta\sigma_N = 2.0\ MPa$ in the Northern sector (Cervialto Fault area, the initial rupturing segment of the 1980 earthquake) and $\Delta\sigma_S = 2.8\ MPa$ in the Southern Sector (San Gregorio Magno Fault area, i.e., on the second rupturing segment of the 1980 earthquake). Tomographic images in velocity (Amoroso et al. 2014, Improta et al. 2014, Vassallo et al. 2016) and anelastic attenuation (Qp, Qs; Amoroso et al. 2017) coupled with rock physics modelling indicate the presence of pressurized fluids in the area of microseismicity. Differences in the stress drops between the two areas could be associated with the different fluid content and fraction. In the Southern sector rock physics modelling indicates the presence of a mixture brine-CO2 (Amoroso et al. 2017). The large, extended low Vp/Vs anomaly in tomographic images in the northern sector indicates a pressurized reservoir of fluids, associated with the large natural emission of low-temperature CO2 at the Mefite d'Ansanto, Rocca San Felice site (Chiodini et al. 2010).

Several studies in the area indicate a correlation between shallow stress changes in the karst aquifer induced by hydrological loading via the poroelastic response of the rocks and deep seismicity (D'Agostino et al. 2018). Although most of the sequences occurred during the maximum aquifer charge, we cannot infer a clear link between stress changes in the shallow water table and the occurrence of the sequences. However, the small amount of stress perturbation that propagates at depth (D'Agostino et al., 2018) compared to the large stress drops retrieved during sequences may indicate an elastic coupling between the shallow Mesozoic carbonates and the underlying Apulian platform beneath the mélange, and a critical state of these small patches, that are prone to generate the sequences with a stress excess that is only a few percent of the stress drop required to nucleate events.

When mapping the stress change on the fault plane associated with the sequences, most of the events appear connected, indicating that the sequences ruptured single patches along the fault plane. The inter-event distance, compared to the size of the events, suggests that the dominant triggering mechanism within the sequences is static stress transfer, that allows the nucleation of individual events in the sequence. Nevertheless, an important feature retrieved here is that the distribution of the events is not isotropic around the main events of the sequences, but small events tend to align dominantly along the dip direction, which also corresponds to the slip direction, for normal faults. Specific patterns for sequences along the direction of the slip have been observed in strike-slip environments (Rubin et al. 1999, Shearer 2002). Lineation of the seismicity along the major faults in California have been interpreted as the boundary between locked and creeping domains (Rubin et al. 1999, Rubinstein and Beroza 2007). In the normal fault environment of Southern Apennines also, evolution of the seismicity during the sequences is controlled by slip and cannot be explained by the anisotropic stress release after the event (Andrews 1980, see also the stress changes of Figure 6). Fault roughness, modulated by repeated stick slip episodes may determine predominant patterns at the scale of the microseismicity observed here ($10 - 100m$), with striations mainly oriented along the dip direction (Candela et al. 2011). Corrugated faults behave as geometrical asperities and can localize deformation hosting stick-slip episodes at small scales (few centimeters of slip) (Resor and Meer 2009). Fault roughness and geometrical barriers at this scale may also impede small events from growing into larger magnitude earthquakes (Sagy et al. 2007, Marshall and Morris 2012). These strips can also favor upward migration of fluids, although we cannot discern a signature of diffusion-dominated processes from the space-time evolution of the sequences.

The occurrence of aseismic slip episodes nearby the lineations could also be the cause for the along-dip evolution of the seismicity and might explain the longer extent compared to the released seismic moment. Aseismic transients have been already observed in normal fault environments during the occurrence of larger seismic sequences (Gualandi et al. 2017, Kaviris et al. 2021). However, for the sequences analyzed here, geodetic data has not detected aseismic transients at this space-time scale during the sequences analyzed in this study.

The Rocca San Felice sequence shows the activation of two parallel clusters, oriented along the dip direction, but about 5 km apart. The two clusters featured main events of similar magnitude (M_l 3.0 and M_l 2.8, respectively), a kilometric size extension along the dip (4 km and 2 km), with the first evolving preferentially up-dip, the second one downdip. The second cluster was activated about two days after the first sequence. As shown in Figure 6, the stress perturbation associated with the first sequence cannot be responsible for the activation of the second patch. Also, the lack of seismicity between the two segments does not support the hypothesis of fluid migration as responsible for triggering the second cluster. According to the rate of occurrence of independent events with $M_l > 2.5$ in the northern part of the region ($\lambda = 2.1 * 10^{-3} ev/day$), we estimated the probability of occurrence of two independent events within 2 days as about 0.4%.

We also tested the hypothesis of aseismic slip between the two seismicity clusters of this sequence. We assess the evolution of the displacement at the three closest GPS stations SNAL, MTMR, ANG1, the first two belonging to the INGV-RING network, the latter to the Regione Campania. The time series of daily coordinates (see D'Agostino et al., 2020 for details of GPS data processing) at the three stations have been checked for possible offsets across the seismic sequence. Evaluating the average positions in North, East and vertical coordinates, before and after the Rocca San Felice sequence, we could not find significant static offsets within the estimated error (Figure 7).

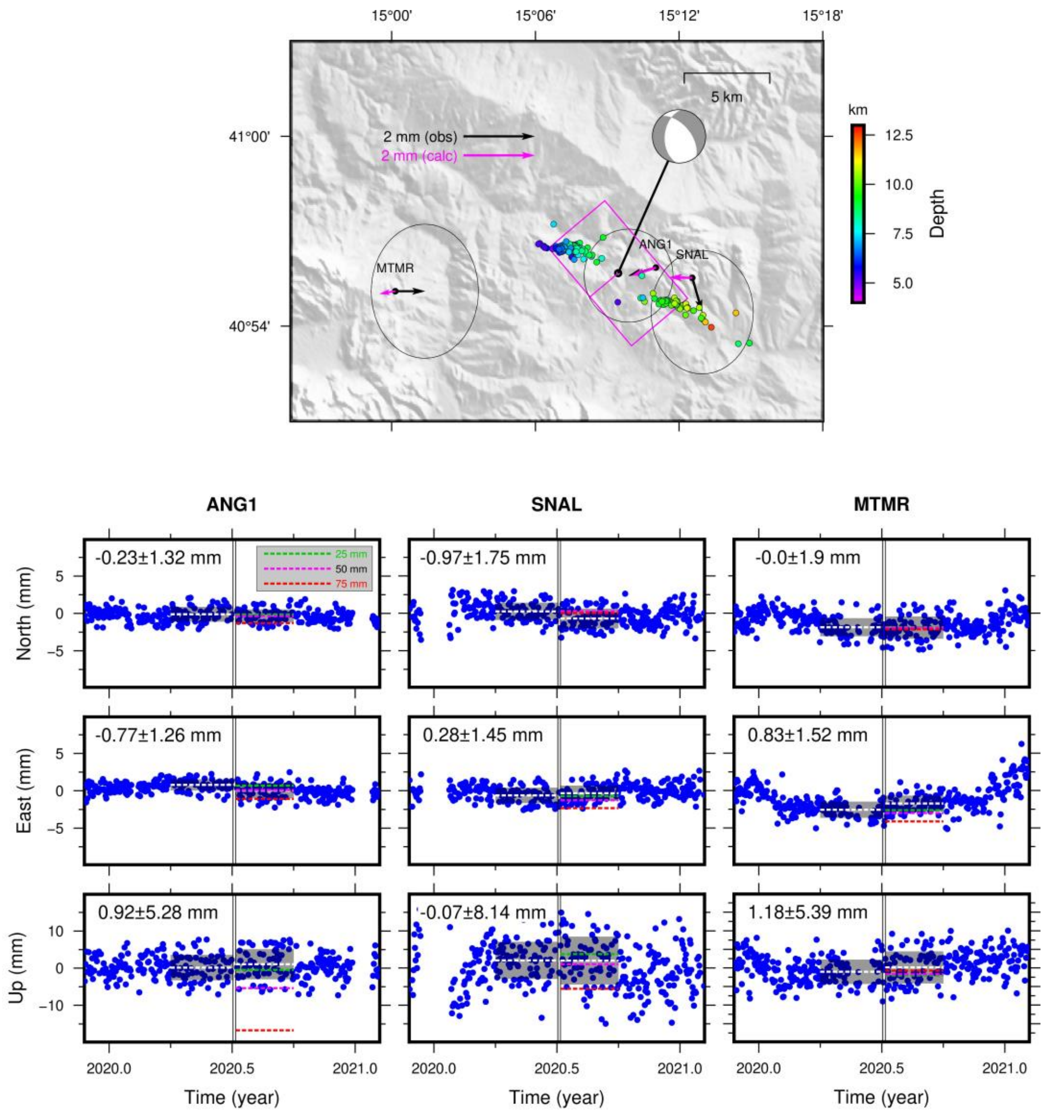

Figure 7) Upper panel: map of the GPS stations near the Rocca San Felice seismic sequence and associated displacements. The vectors show the horizontal displacements with one sigma error ellipses, from the static offset during the seismic sequence. Circles represent events of the sequence color-coded with depth. Three different synthetic scenarios were evaluated assuming increasing slip (25, 50 ,75 mm), with geometry and kinematics from Festa et al., 2021. The surface displacements produced by a slip of 50 mm on the fault drawn with purple lines is shown in the map (purple arrows). Lower panel. GPS position time series and average positions (white dashed lines) before and after the seismic sequence, with 1-sigma error shown with grey shading. Calculated displacements are also shown (dashed lines) for the 25mm (green), 50mm (purple) and 75 mm (red) dislocation scenarios.

We assessed the maximum average slip allowed on a deep dislocation whose displacement on the surface would not emerge from the noise level at the three GPS stations. We centered the potential aseismic dislocation between the two clusters and used the fault geometry and kinematics inferred by the composite focal mechanism solution of Festa et al. (2021) and calculated the surface displacements using the Okada techniques (Okada 1992). We tested a range of uniform slip on the dislocation between 25 and 75 mm, assuming constant strain drop of 10^{-5}. The relatively deep position of the dislocation centroid between the two clusters (~8 km) allows slip on the deep dislocations up to 50 mm without detection at the surface (Figure 7). For slip larger than 50 mm the non-linear increase of cumulative seismic moment determines surface displacements outside the range of allowed offsets. Thus, an aseismic event of M_w ~5.0 could have occurred during the sequence, transferring stress across the two asperities without producing a signal that would have been visible at the GPS stations.

6 Conclusions

In this work we presented a comprehensive analysis of seismic sequences through accurate earthquake location and source parameters estimation of enhanced catalogs (Scotto di Uccio et al. 2023). Selecting machine learning and cross-correlation phase arrival times, we retrieved double difference locations for ~30% of the events. The relocated seismicity revealed that seismic sequences involve kilometric-scale structures, featuring a NW-SE dip and larger extent than expected from the magnitude of the mainshocks. While location of microseismicity usually relies on the use of records from velocimetric sensors, in this work the resolution of hypocenters benefited from phase arrival times determined on accelerometers located close to the main events of the sequences. Accelerometers can thus provide important arrival time information that is comparable in quality to velocimetric stations, improving the location results. For the relocated earthquakes, we estimated the source parameters (seismic moment M_0, corner frequency f_c) through a probabilistic inversion of the displacement spectra (Supino et al. 2019), and the resulting source size r and stress drop $\Delta\sigma$, assuming the generalized Brune model, finally mapping the stress change along the fault plane. We estimated the moment magnitude for 60% of the relocated events and we resolved the corner frequencies only for earthquakes with $M_w > 2.0$, using low-magnitude events as EGFs. We observed $\Delta\sigma$ spanning the range [0.9 – 5.4] MPa, within the interval proposed for earthquakes in the Irpinia area (Picozzi et al. 2021) and source radius for the main events varies from 105 – 235 m. We observed differences in the stress drops associated with sequences, with an increase of the stress drop from North to South in the Irpinia region, likely associated to the different fluid content and fraction. When mapping the stress change on the fault plane associated with the sequences, most of the events appear connected, indicating that the sequences ruptured single, contiguous patches along the fault plane. The inter-event distance, compared to the size of the events, suggests that the dominant triggering mechanism within the sequences is the (static) stress transfer, that allows the nucleation of individual events in the sequence. Alignment of events mainly along the dip direction indicates a slip dominated mechanism in the evolution of the seismicity, which could be associated with different fault roughness in the directions of the dip and strikes. Lineations in the definition of the seismicity might indicate aseismic transients occurring at the same time of the sequences. These transients could explain the migration of the seismicity from one cluster to the other one during the Rocca San Felice sequence. Although GPS data from stations located just above the sequence do not contain offsets indicative of such transients, a Mw 5 aseismic event could have occurred at the sequence depth, without producing a signal emerging from the noise.

Open Research

Seismic products from the Irpinia Near Fault Observatory can be accessed through the Irpinia Seismic Network website (https://isnet.unina.it). Seismic data from INFO can be accessed through EIDA portal (https://eida.ingv.it/it/), network code IX or via the EPOS portal (https://www.ics-c.epos-eu.org/). GNSS data are accessible through the INGV website ftp://bancadati2.gm.ingv.it:2121/OUTGOING/RINEX30/RING/. Earthquake relocations were performed using NonLinLoc (https://github.com/alomax/NonLinLoc) and HYPODD (https://www.ldeo.columbia.edu/~felixw/hypoDD.html). Catalogs of the analyzed events are available at the following link: https://zenodo.org/records/10441456 (Scotto di Uccio & Festa, 2023) Maps in Figure 2 and Figure 3 were made using PyGMT (Uieda et al., 2021). Figure 4 and Figure 5 were produced using Matplotlib (Hunter, J.D., 2007). Figure 6 was produced using Matlab.

References

Abercrombie, R. E., & Rice, J. R. (2005). Can observations of earthquake scaling constrain slip weakening?. *Geophysical Journal International*, *162*(2), 406-424.

Abercrombie, R. E. (2015). Investigating uncertainties in empirical Green's function analysis of earthquake source parameters. *Journal of Geophysical Research: Solid Earth*, *120*(6), 4263-4277.

Abercrombie, R. E. (1995). Earthquake source scaling relationships from− 1 to 5 ML using seismograms recorded at 2.5-km depth. *Journal of Geophysical Research: Solid Earth*, *100*(B12), 24015-24036.

Amoroso, O., Ascione, A., Mazzoli, S., Virieux, J., & Zollo, A. (2014). Seismic imaging of a fluid storage in the actively extending Apennine mountain belt, southern Italy. *Geophysical Research Letters*, *41*(11), 3802-3809.

Amoroso, O., Russo, G., De Landro, G., Zollo, A., Garambois, S., Mazzoli, S., ... & Virieux, J. (2017). From velocity and attenuation tomography to rock physical modeling: Inferences on fluid-driven earthquake processes at the Irpinia fault system in southern Italy. *Geophysical Research Letters*, *44*(13), 6752-6760.

Amoruso, A., Crescentini, L., D'Anastasio, E., & De Martini, P. M. (2005). Clues of postseismic relaxation for the 1915 Fucino earthquake (central Italy) from modeling of leveling data. *Geophysical Research Letters*, *32*(22).

Andrews, D. J. (1980). A stochastic fault model: 1. Static case. *Journal of Geophysical Research: Solid Earth*, *85*(B7), 3867-3877.

Bernard, P., & Zollo, A. (1989). The Irpinia (Italy) 1980 earthquake: detailed analysis of a complex normal faulting. *Journal of Geophysical Research: Solid Earth*, *94*(B2), 1631-1647.

Beroza, G. C., Segou, M., & Mostafa Mousavi, S. (2021). Machine learning and earthquake forecasting—next steps. *Nature communications*, *12*(1), 4761.

Boore, D. M., & Boatwright, J. (1984). Average body-wave radiation coefficients. *Bulletin of the Seismological Society of America*, *74*(5), 1615-1621.

Brune, J. N. (1970). Tectonic stress and the spectra of seismic shear waves from earthquakes. *Journal of geophysical research*, *75*(26), 4997-5009.

Cabrera, L., Poli, P., & Frank, W. B. (2022). Tracking the spatio-temporal evolution of foreshocks preceding the Mw 6.1 2009 L'Aquila earthquake. *Journal of Geophysical Research: Solid Earth*, *127*(3), e2021JB023888.

Candela, T., Renard, F., Schmittbuhl, J., Bouchon, M., & Brodsky, E. E. (2011). Fault slip distribution and fault roughness. *Geophysical Journal International*, *187*(2), 959-968.

Chamberlain, C. J., Hopp, C. J., Boese, C. M., Warren-Smith, E., Chambers, D., Chu, S. X., ... & Townend, J. (2018). EQcorrscan: Repeating and near-repeating earthquake detection and analysis in Python. *Seismological Research Letters*, *89*(1), 173-181.

Chen, X., Shearer, P. M., & Abercrombie, R. E. (2012). Spatial migration of earthquakes within seismic clusters in Southern California: Evidence for fluid diffusion. *Journal of Geophysical Research: Solid Earth*, *117*(B4).

Chiaraluce, L., Valoroso, L., Anselmi, M., Bagh, S., & Chiarabba, C. (2009). A decade of passive seismic monitoring experiments with local networks in four Italian regions. *Tectonophysics*, *476*(1-2), 85-98.

Chiaraluce, L., Festa, G., Bernard, P., Caracausi, A., Carluccio, I., Clinton, J. F., ... & Sokos, E. (2022). The Near Fault Observatory community in Europe: a new resource for faulting and hazard studies. *Annals of Geophysics*, *65*(3), DM316.

Chiodini, G., Granieri, D., Avino, R., Caliro, S., Costa, A., Minopoli, C., & Vilardo, G. (2010). Non-volcanic CO2 Earth degassing: Case of Mefite d'Ansanto (southern Apennines), Italy. *Geophysical Research Letters*, *37*(11).

Cianetti, S., Bruni, R., Gaviano, S., Keir, D., Piccinini, D., Saccorotti, G., & Giunchi, C. (2021). Comparison of deep learning techniques for the investigation of a seismic sequence: An application to the 2019, Mw 4.5 Mugello (Italy) earthquake. *Journal of Geophysical Research: Solid Earth*, *126*(12), e2021JB023405.

D'Agostino, N., Silverii, F., Amoroso, O., Convertito, V., Fiorillo, F., Ventafridda, G., & Zollo, A. (2018). Crustal deformation and seismicity modulated by groundwater recharge of karst aquifers. *Geophysical Research Letters*, *45*(22), 12-253.

D'Agostino, N., Métois, M., Koci, R., Duni, L., Kuka, N., Ganas, A., Georgiev, A., Jouanne,F., Kaludjerovic, N., & Kandić, R. (2020). Active crustal deformation and rotations in the southwestern Balkans from continuous GPS measurements. *Earth and Planetary Science Letters*, 539, 116246.

Daout, S., D'Agostino, N., Pathier, E., Socquet, A., Lavé, J., Doin, M.P., Riesner, M., & Benedetti, L. (2023) Along-strike variations of strain partitioning within the Apennines determined from large-scale multi-temporal InSAR analysis. *Tectonophysics*, 867, 230076, ISSN 0040-1951, https://doi.org/10.1016/j.tecto.2023.230076.

De Landro, G., Amoroso, O., Stabile, T. A., Matrullo, E., Lomax, A., & Zollo, A. (2015). High-precision differential earthquake location in 3-D models: evidence for a rheological barrier controlling the microseismicity at the Irpinia fault zone in southern Apennines. *Geophysical Supplements to the Monthly Notices of the Royal Astronomical Society*, *203*(3), 1821-1831.

Deichmann, N. (2017). Theoretical basis for the observed break in ML/M w scaling between small and large earthquakes. *Bulletin of the Seismological Society of America*, *107*(2), 505-520.

Deschamps, A., & King, G. C. P. (1983). The Campania-Lucania (southern Italy) earthquake of 23 November 1980. *Earth and Planetary Science Letters*, *62*(2), 296-304.

Edwards, B., Kraft, T., Cauzzi, C., Kästli, P., & Wiemer, S. (2015). Seismic monitoring and analysis of deep geothermal projects in St Gallen and Basel, Switzerland. *Geophysical Journal International*, *201*(2), 1022-1039.

Festa, G., Adinolfi, G. M., Caruso, A., Colombelli, S., De Landro, G., Elia, L., ... & Zollo, A. (2021). Insights into mechanical properties of the 1980 Irpinia fault system from the analysis of a seismic sequence. *Geosciences*, *11*(1), 28.

Gualandi, A., Nichele, C., Serpelloni, E., Chiaraluce, L., Anderlini, L., Latorre, D., ... & Avouac, J. P. (2017). Aseismic deformation associated with an earthquake swarm in the northern Apennines (Italy). *Geophysical Research Letters*, *44*(15), 7706-7714.

Gulia, L., & Wiemer, S. (2019). Real-time discrimination of earthquake foreshocks and aftershocks. *Nature*, *574*(7777), 193-199.

Hawthorne, J. C., & Bartlow, N. M. (2018). Observing and modeling the spectrum of a slow slip event. *Journal of Geophysical Research: Solid Earth*, *123*(5), 4243-4265.

Herrmann, M., & Marzocchi, W. (2021). Inconsistencies and lurking pitfalls in the magnitude–frequency distribution of high-resolution earthquake catalogs. *Seismological Research Letters*, *92*(2A), 909-922.

Herrmann, M., Piegari, E., & Marzocchi, W. (2022). Revealing the spatiotemporal complexity of the magnitude distribution and b-value during an earthquake sequence. *Nature Communications*, *13*(1), 5087.

Hunter, J. D. (2007). Matplotlib: A 2D graphics environment. *Computing in science & engineering*, *9*(03), 90-95. [Software]

Iannaccone, G., Zollo, A., Elia, L., Convertito, V., Satriano, C., Martino, C., Festa, G., Lancieri, M., Bobbio, A., Stabile, T. A., Vassallo, M. & Emolo, A., 2010. A prototype system for earthquake early-warning and alert management in southern Italy. Bull. Earthq. Eng., 8(5), 11051129.

Improta, L., De Gori, P., & Chiarabba, C. (2014). New insights into crustal structure, Cenozoic magmatism, CO2 degassing, and seismogenesis in the southern Apennines and Irpinia region from local earthquake tomography. *Journal of Geophysical Research: Solid Earth*, *119*(11), 8283-8311.

Kaviris, G., Elias, P., Kapetanidis, V., Serpetsidaki, A., Karakonstantis, A., Plicka, V., ... & Bernard, P. (2021). The western Gulf of Corinth (Greece) 2020–2021 seismic crisis and cascading events: First results from the Corinth Rift Laboratory Network. *The Seismic Record*, *1*(2), 85-95.

Keilis-Borok, V. (1959). On estimation of the displacement in an earthquake source and of source dimensions. *Annali di geofisica*, *12*(2), 205-214.

Liu, F., Xue, S., Wu, J., Zhou, C., Hu, W., Paris, C., ... & Yu, P. S. (2020). Deep learning for community detection: progress, challenges and opportunities. *arXiv preprint arXiv:2005.08225*.

Lomax, A., Virieux, J., Volant, P., & Berge-Thierry, C. (2000). Probabilistic earthquake location in 3D and layered models: Introduction of a Metropolis-Gibbs method and comparison with linear locations. *Advances in seismic event location*, 101-134.

Lomax, A. (2020). Absolute location of 2019 Ridgecrest seismicity reveals a shallow Mw 7.1 hypocenter, migrating and pulsing Mw 7.1 foreshocks, and duplex Mw 6.4 ruptures. *Bulletin of the Seismological Society of America*, *110*(4), 1845-1858.

Madariaga, R. (1976). Dynamics of an expanding circular fault. *Bulletin of the Seismological Society of America*, *66*(3), 639-666.

Mancini, S., Segou, M., Werner, M. J., Parsons, T., Beroza, G., & Chiaraluce, L. (2022). On the Use of High-Resolution and Deep-Learning Seismic Catalogs for Short-Term Earthquake Forecasts: Potential Benefits and Current Limitations. *Journal of Geophysical Research: Solid Earth*, *127*(11), e2022JB025202.

Marshall, S. T., & Morris, A. C. (2012). Mechanics, slip behavior, and seismic potential of corrugated dip-slip faults. *Journal of Geophysical Research: Solid Earth*, *117*(B3).

Marzocchi, W., Spassiani, I., Stallone, A., & Taroni, M. (2020). How to be fooled searching for significant variations of the b-value. *Geophysical Journal International*, *220*(3), 1845-1856.

Matrullo, E., De Matteis, R., Satriano, C., Amoroso, O., & Zollo, A. (2013). An improved 1-D seismic velocity model for seismological studies in the Campania–Lucania region (Southern Italy). *Geophysical Journal International*, *195*(1), 460-473.

Michele, M., Chiaraluce, L., Di Stefano, R., & Waldhauser, F. (2020). Fine-scale structure of the 2016–2017 Central Italy seismic sequence from data recorded at the Italian National Network. *Journal of Geophysical Research: Solid Earth*, *125*(4), e2019JB018440.

Mori, J., & Frankel, A. (1990). Source parameters for small events associated with the 1986 North Palm Springs, California, earthquake determined using empirical Green functions. *Bulletin of the Seismological Society of America*, *80*(2), 278-295.

Mousavi, S. M., Ellsworth, W. L., Zhu, W., Chuang, L. Y., & Beroza, G. C. (2020). Earthquake transformer—an attentive deep-learning model for simultaneous earthquake detection and phase picking. *Nature communications*, *11*(1), 3952.

Münchmeyer, J., Woollam, J., Rietbrock, A., Tilmann, F., Lange, D., Bornstein, T., ... & Soto, H. (2022). Which picker fits my data? A quantitative evaluation of deep learning based seismic pickers. *Journal of Geophysical Research: Solid Earth*, *127*(1), e2021JB023499.

Okada, Y.(1992) Internal deformation due to shear and tensile faults in a half-space. *Bulletin of the Seismological Society of America*, 82 (2), 1018–1040. https://doi.org/10.1785/BSSA0820021018

Oth, A., Wenzel, F., & Radulian, M. (2007). Source parameters of intermediate-depth Vrancea (Romania) earthquakes from empirical Green's functions modeling. *Tectonophysics*, *438*(1-4), 33-56.

Palo, M., Picozzi, M., De Landro, G., & Zollo, A. (2023). Microseismicity clustering and mechanic properties reveal fault segmentation in southern Italy. *Tectonophysics*, *856*, 229849.

Park, Y., Mousavi, S. M., Zhu, W., Ellsworth, W. L., & Beroza, G. C. (2020). Machine-learning-based analysis of the Guy-Greenbrier, Arkansas earthquakes: A tale of two sequences. *Geophysical Research Letters*, *47*(6), e2020GL087032.

Park, Y., Beroza, G. C., & Ellsworth, W. L. (2022). Basement fault activation before larger earthquakes in Oklahoma and Kansas. *The Seismic Record*, *2*(3), 197-206.

Park, Y., Beroza, G. C., & Ellsworth, W. L. (2023). A mitigation strategy for the prediction inconsistency of neural phase pickers. *Seismological Society of America*, *94*(3), 1603-1612.

Picozzi, M., Bindi, D., Festa, G., Cotton, F., Scala, A., & D'Agostino, N. (2022). Spatiotemporal evolution of microseismicity seismic source properties at the Irpinia Near-Fault Observatory, Southern Italy. *Bulletin of the Seismological Society of America*, *112*(1), 226-242.

Poupinet, G., Ellsworth, W. L., & Frechet, J. (1984). Monitoring velocity variations in the crust using earthquake doublets: An application to the Calaveras Fault, California. *Journal of Geophysical Research: Solid Earth*, *89*(B7), 5719-5731.

Prieto, G. A., Shearer, P. M., Vernon, F. L., & Kilb, D. (2004). Earthquake source scaling and self-similarity estimation from stacking P and S spectra. *Journal of Geophysical Research: Solid Earth*, *109*(B8).

Resor, P. G., & Meer, V. E. (2009). Slip heterogeneity on a corrugated fault. *Earth and Planetary Science Letters*, *288*(3-4), 483-491.

Ross, Z. E., Trugman, D. T., Hauksson, E., & Shearer, P. M. (2019). Searching for hidden earthquakes in Southern California. *Science*, *364*(6442), 767-771.

Ross, Z. E., Cochran, E. S., Trugman, D. T., & Smith, J. D. (2020). 3D fault architecture controls the dynamism of earthquake swarms. *Science*, *368*(6497), 1357-1361.

Rovida, A. N., Locati, M., Camassi, R. D., Lolli, B., & Gasperini, P. (2019). Catalogo parametrico dei terremoti italiani cpti15, versione 2.0.

Rubin, A. M., Gillard, D., & Got, J. L. (1999). Streaks of microearthquakes along creeping faults. *Nature*, *400*(6745), 635-641.

Rubinstein, J. L., & Beroza, G. C. (2007). Full waveform earthquake location: Application to seismic streaks on the Calaveras fault, California. *Journal of Geophysical Research: Solid Earth*, *112*(B5).

Sagy, A., Brodsky, E. E., & Axen, G. J. (2007). Evolution of fault-surface roughness with slip. *Geology*, *35*(3), 283-286.

Schaff, D. P., Bokelmann, G. H., Ellsworth, W. L., Zanzerkia, E., Waldhauser, F., & Beroza, G. C. (2004). Optimizing correlation techniques for improved earthquake location. *Bulletin of the Seismological Society of America*, *94*(2), 705-721.

Scholz, C. H. (2015). On the stress dependence of the earthquake b value. *Geophysical Research Letters*, *42*(5), 1399-1402.

Scotto di Uccio, F., Scala, A., Festa, G., Picozzi, M., & Beroza, G. C. (2023). Comparing and integrating artificial intelligence and similarity search detection techniques: application to seismic sequences in Southern Italy. *Geophysical Journal International*, *233*(2), 861-874.

Scotto di Uccio, F., & Festa, G. (2023). Catalog of relocated seismic sequences in Irpinia [Data set]. Zenodo. https://doi.org/10.5281/zenodo.10441456

Shearer, P. M. (2002). Parallel fault strands at 9-km depth resolved on the Imperial fault, southern California. *Geophysical Research Letters*, *29*(14), 19-1.

Silverii, F., D'Agostino, N., Borsa, A. A., Calcaterra, S., Gambino, P., Giuliani, R., & Mattone, M. (2019). Transient crustal deformation from karst aquifers hydrology in the Apennines (Italy). *Earth and Planetary Science Letters*, *506*, 23-37.

Simon, V., Kraft, T., Diehl, T., & Tormann, T. (2021). Possible Precursory Slow-Slip to Two ML∼3 Mainevents of the Diemtigen Microearthquake Sequence, Switzerland. *Geophysical Research Letters*, *48*(19), e2021GL093783.

Spallarossa, D., Cattaneo, M., Scafidi, D., Michele, M., Chiaraluce, L., Segou, M., & Main, I. G. (2021). An automatically generated high-resolution earthquake catalog for the 2016–2017 Central Italy seismic sequence, including P and S phase arrival times. *Geophysical Journal International*, *225*(1), 555-571.

Stabile, T. A., Satriano, C., Orefice, A., Festa, G., & Zollo, A. (2012). Anatomy of a microearthquake sequence on an active normal fault. *Scientific reports*, *2*(1), 410.

Stucchi, M., Meletti, C., Montaldo, V., Crowley, H., Calvi, G. M., & Boschi, E. (2011). Seismic hazard assessment (2003–2009) for the Italian building code. *Bulletin of the Seismological Society of America*, *101*(4), 1885-1911.

Sugan, M., Campanella, S., Chiaraluce, L., Michele, M., & Vuan, A. (2023). The unlocking process leading to the 2016 Central Italy seismic sequence. *Geophysical Research Letters*, *50*(5), e2022GL101838.

Supino, M., Festa, G., & Zollo, A. (2019). A probabilistic method for the estimation of earthquake source parameters from spectral inversion: application to the 2016–2017 Central Italy seismic sequence. *Geophysical Journal International*, *218*(2), 988-1007.

Supino, M., Poiata, N., Festa, G., Vilotte, J. P., Satriano, C., & Obara, K. (2020). Self-similarity of low-frequency earthquakes. *Scientific Reports*, *10*(1), 6523.

Tan, Y. J., Waldhauser, F., Ellsworth, W. L., Zhang, M., Zhu, W., Michele, M., ... & Segou, M. (2021). Machine-learning-based high-resolution earthquake catalog reveals how complex fault structures were activated during the 2016–2017 Central Italy sequence. *The Seismic Record*, *1*(1), 11-19.

Trugman, D. T., & Shearer, P. M. (2017). GrowClust: A hierarchical clustering algorithm for relative earthquake relocation, with application to the Spanish Springs and Sheldon, Nevada, earthquake sequences. *Seismological Research Letters*, *88*(2A), 379-391.

Uieda, L., Tian, D., Leong, W. J., Toney, L., Schlitzer, W., Yao, J., Grund, M., Jones, M., 646 Materna, K., Newton, T., Ziebarth, M., & Wessel, P. (2021). PyGMT: A Python 647 interface for the Generic Mapping Tools (v0.3.1) [Software]

Vassallo, M., Festa, G., Bobbio, A., & Serra, M. (2016). Low shear velocity in a normal fault system imaged by ambient noise cross correlation: The case of the Irpinia fault zone, Southern Italy. *Journal of Geophysical Research: Solid Earth*, *121*(6), 4290-4305.

Vuan, A., Sugan, M., Amati, G., & Kato, A. (2018). Improving the detection of low-magnitude seismicity preceding the Mw 6.3 L'Aquila earthquake: Development of a scalable code based on the cross correlation of template earthquakes. *Bulletin of the Seismological Society of America*, *108*(1), 471-480.

Vuan, A., Brondi, P., Sugan, M., Chiaraluce, L., Di Stefano, R., & Michele, M. (2020). Intermittent slip along the Alto Tiberina low-angle normal fault in central Italy. *Geophysical Research Letters*, *47*(17), e2020GL089039.

Waldhauser, F., & Ellsworth, W. L. (2000). A double-difference earthquake location algorithm: Method and application to the northern Hayward fault, California. *Bulletin of the seismological society of America*, *90*(6), 1353-1368.

Waldhauser, F. (2001). hypoDD--A program to compute double-difference hypocenter locations.

Waldhauser, F., Michele, M., Chiaraluce, L., Di Stefano, R., & Schaff, D. P. (2021). Fault planes, fault zone structure and detachment fragmentation resolved with high-precision aftershock locations of the 2016–2017 central Italy sequence. *Geophysical Research Letters*, *48*(16), e2021GL092918.

Westaway, R., & Jackson, J. (1987). The earthquake of 1980 November 23 in Campania—Basilicata (southern Italy). *Geophysical Journal International*, *90*(2), 375-443.

Yoon, C. E., Yoshimitsu, N., Ellsworth, W. L., & Beroza, G. C. (2019). Foreshocks and mainshock nucleation of the 1999 M w 7.1 Hector Mine, California, Earthquake. *Journal of Geophysical Research: Solid Earth*, *124*(2), 1569-1582.

Zhu, W., & Beroza, G. C. (2019). PhaseNet: A deep-neural-network-based seismic arrival-time picking method. *Geophysical Journal International*, *216*(1), 261-273.

Zollo, A., Orefice, A., & Convertito, V. (2014). Source parameter scaling and radiation efficiency of microearthquakes along the Irpinia fault zone in southern Apennines, Italy. *Journal of Geophysical Research: Solid Earth*, *119*(4), 3256-3275.